Crack Path Predictions in Heterogeneous Media by Machine Learning

M. Worthington, H.B. Chew*

Department of Aerospace Engineering, University of Illinois at Urbana-Champaign, Urbana IL 61801, USA

*Author to whom all correspondence should be addressed. Email: hbchew@illinois.edu

Abstract

The interaction between stress fields at the crack-tip and nearby microstructural heterogeneities influences the crack path, and in turn, the effective fracture toughness of a material. In this paper, we assess the ability of artificial neural networks (ANNs) for machine learning to predict the crack paths from given initial void defect distributions in the material, and to provide insights into the underlying crack growth mechanics. Our ANN accurately captures the process zone size, crack growth sequence, and resulting crack patterns in the simplistic case where the proximity of voids to the crack-tip forms the criterion for crack advance. In a ductile medium, pre-existing voids grow with deformation and link up with the primary crack either contiguously or through the formation of multiple unconnected damage zones. The complex crack patterns for both these ductile fracture processes are successfully captured by an ANN, trained on the cracking sequences in a micromechanics-based ductile fracture model containing two size-scales of voids. In addition, the ANN architecture is capable of predicting stochastic crack growth, by providing a multiplicity of possible crack paths, along with a quantified likelihood of each path. Results further demonstrate the utility of autonomous crack path predictions in enabling fracture-by-design.

Keywords: Artificial neural networks; stochastic crack growth; voids; micromechanics model; crack patterns

1. Introduction

The field of fracture mechanics has seen remarkable advances since its inception a century ago, but predicting the path chosen by a crack as it propagates through a heterogeneous medium remains a long-standing challenge. In the context of brittle materials, two prevailing theories have emerged. The first assumes that the crack tries to minimize its shear (mode II) component by rotating to achieve a pure opening mode with a symmetrical stress distribution about its local axis (mode I) (Goldstein and Salganik, 1974; Cotterell and Rice, 1980; Fleck et al., 1991). The second postulates that the crack will choose the direction that maximizes the dissipated strain energy at its tip (Wu, 1978; Slepyan, 1993; Francfort and Marigo, 1998). Both these criteria are in reasonably good agreement with experimental data over a wide range of loadings (Erdogan and Sih, 1963; Adda-Bedia, 2005; Rozen-Levy et al., 2020). In ductile materials, however, the direction of crack growth depends on two competing failure mechanisms: microvoid coalescence and shear localization (McVeigh et al., 2007; Tekoglu et al., 2015). The former dominates under mode I loading, while a transition to the latter occurs with increasing shear. The mode mixity at which this transition occurs varies with material, and is dependent on the work hardening, as well as the distribution and size of inclusions. As such, predicting the crack paths in a ductile medium is more challenging than in a brittle medium.

Computational fracture mechanics models are now widely used to elucidate the crack paths and fracture patterns in both brittle and ductile media. Historically, a major research thrust has been describing the mechanistic process of material separation within the fracture process zone on the microscale (Hutchinson and Evans, 2000). With corresponding advances in high-resolution microscopy imaging and accompanying atomistic simulations, the micromechanisms underpinning damage evolution and crack propagation are more or less well-defined for a wide range of engineering materials (Prakash et al., 2009; Murali et al., 2011; Kim et al., 2013; Li and Chew, 2017; Xie et al., 2022). For example, it is now well-accepted that stress and strain heterogeneities – which arise in the vicinity of grain boundaries, inclusions, second phase particles, or even surface roughness – are precursors to fracture initiation in metals (Chan, 2009; Abuzaid et al., 2013; VanSickle, 2020). To incorporate these microscopic aspects of the failure process, studies have modeled the complicated fracture process zone with cohesive zone laws (Tvergaard and Hutchinson, 1992; Williams and Hadavinia, 2002; Hong et al., 2009; Chew et al., 2009; Chew, 2014; Huy et al., 2022), or with computational cell elements governed by porous constitutive material relations such as the Gurson model (Gurson, 1977; Xia and Shih, 1995). A major limitation is that the process zone and hence the crack path has to be defined a priori, and as such cannot capture the effects of crack branching, deflection, and merging. This has motivated the development of phase-field models for fracture, which regularizes the topology of the sharp crack as a diffuse damage zone instead of a discontinuity (Miehe et al., 2016; Tanne et al., 2018; Sargado et al., 2018; Tran and Chew, 2022).

Predicting the crack path from a given distribution of defects is a forward problem, which can be resolved with the aforementioned computational fracture models in finite element method (FEM). However, optimizing the distribution of defects to achieve the desired crack path is an inverse problem that necessitates *fast* predictions of the crack path (output) from given spatial distributions of defects (input). Data-driven approaches using machine learning are a promising way to achieve this. At the macroscale, studies have used machine learning to uncover history- and microstructure-dependent constitutive models of general materials and material classes (Mozaffar et al., 2019), as well as macroscopic "Paris-Law"-type nonlinear relationships between fatigue crack growth rates and the range of stress intensity factor (Zhu et al., 2018). At the microscale, machine learning has facilitated the predictions of grain boundary energy and stresses (Homer et al., 2019; Huber et al., 2018; Cui and Chew, 2022), as well as the identification of relevant local microstructural features for stress hotspots and fatigue cracking at the sub-grain level (Rovinelli et al., 2018; Pierson et al., 2019). Through machine learning, studies have recently quantified the internal stress evolution as well as the crack link-up process during fracture in brittle materials (Moore et al., 2018; Hunter et al., 2019; Wang et al., 2021). Recent successes in predicting brittle fracture using molecular dynamics (MD)-derived training data lends promise to the use of the neural network approach for crack prediction (Hsu et al., 2020; Buehler, 2022). In addition, such a neural network model with a genetic algorithm approach has been used to predict and design for desired crack paths in polycrystalline 2D materials (Lew and Buehler, 2021). However, predictions of the fracture patterns and cracking sequences from initial defect distributions at the microstructural level in heterogeneous ductile materials have remained elusive.

In this work, we highlight the successes and limitations of artificial neural networks (ANNs) for machine learning in predicting the crack paths from given initial void defect distributions in heterogeneous brittle and ductile materials. Section 2 details the architecture of the ANN, and we investigate the ability of this ANN to capture the process zone size, crack growth sequence, and resulting crack patterns for the simplistic case where the proximity of voids to the crack-tip forms the criterion for crack advance, akin to a brittle-like media. In a ductile media, pre-existing voids grow with deformation and interact with each other and/or with the propagating crack-tip. Section 3 extends the crack path predictions to a ductile media, where we generate the datasets to train the ANN from a micromechanics-based ductile fracture model containing two size-scales of voids (Yue et al., 2020; Muro-Barrios et al., 2022). In Section 4, we discuss the integration of our ANN with a Genetic Algorithm (GA) to optimize the placement of voids within the process zone to achieve the desired crack path. Section 5 concludes with a summary.

2. Artificial Neural Networks for Brittle Media

Earlier work using convolutional, attention, and diffusion models (among others) have been shown to introduce a physical basis for neural network models and thereby making the resulting neural network architecture broadly applicable, and predictive (Hsu et al., 2020; Lew and Buehler, 2021; Buehler, 2022). Here, we adopt feed-forward artificial neural networks (ANNs) with a multilayer perceptron architecture to predict the crack propagation direction (Fig. 1a-ii) from the spatial distribution of defects in the form of voids ahead of the current crack-tip (Fig. 1a-i). While prior studies have demonstrated the ability of convolutional neural networks to predict stress concentrations or stress hotspots which are precursors for crack growth (Rovinelli et al., 2018; Pierson et al., 2019), the use of a relatively simple ANN architecture (Fig. 1b) allows us to bypass intermediaries such as stress concentration to achieve a one-to-one correspondence between the location of voids surrounding a crack-tip and the prediction of the crack growth direction with limited training data, which is the goal of this work. The complex crack-void interaction mechanisms within the region of damage around the crack-tip, i.e., the fracture process zone, typically controls the crack propagation direction. For each crack growth sequence, we represent this process zone with an $n \times n$ grid of elements (bold solid line region) directly ahead of the current crack-tip, and adopt binary strings of “1” and “0” to denote damage (void-containing) and background (void-free) elements, respectively (Fig. 1a) – void defects outside this process zone have no influence on crack advance at the current step.

The ANN comprises of an input layer, several hidden layer(s), as well as an output layer (Fig. 1b); each layer has varying number of nodes. In our crack path prediction, the number of nodes in the input layer correlates directly with the number of elements comprising the process zone ahead of the current crack-tip (bold solid line region in Fig. 1a-i), while the number of nodes in the output layer corresponds to the number of possible crack growth directions (arrows in Fig. 1a-ii). The nodes within each hidden layer apply transformations to the previous layer before passing them on to the next layer. We impose a hyperbolic tangent activation function between the input/hidden and successive hidden/hidden layers, and a logistic activation function between the final hidden/output layers. In this fashion, the ANN applies a series of weighting functions and biases to the input data to transform them into the output prediction. During backward propagation, these weights and biases are calibrated to minimize the error computed by a cross-entropy loss function. With the updated weights and biases, the network will predict the new crack propagation direction (forward propagation), correct the weights and biases by passing the error backwards (backward propagation), and iterate until convergence is achieved. Despite the simplicity of this ANN architecture (Fig. 1b), it is able to provide strong physical insights into the process zone characteristics and micromechanical crack growth process when trained on realistic and well-validated fracture models. In particular, the optimized weights of the neural network can provide insights to the relative importance of porosity locations surrounding the crack-tip pertaining to the crack propagation mechanics, and can quantify fundamental fracture characteristics, including the size and shape of the crack-tip fracture process zone.

2.1 Crack growth datasets

Brittle fracture has been shown to be governed by nanoscale void coalescence (Guilloteau et al., 1996; Van Brutzel et al., 2002). The macroscopic response of a brittle fracture specimen is often characterized by a lack of plastic deformation, despite substantial plastic deformations developing near the micro-crack-tip (Muralidharan et al., 2005). Thus, in brittle fracture, the presence of defects in the form of voids proximate to the crack tip may still drive crack growth towards these defects. However, damage associated with this crack propagation process is strictly limited to a narrow region surrounding the crack path, without deformation or distortion of the surrounding material (Rice, 1968). For illustration purposes, we reproduce in Fig. 1c the plastic wake contours overlaid on a heat tinted optical microstructural image of Ti-6Al-4V fabricated by additive manufacturing (VanSickle et al., 2020). Void-like processing defects of ~30 μm in diameter are observed in the optical microstructural image, and the crack path tends to propagate towards voids (indicated by white arrows) which are proximate to the crack-tip. Thus, we adopt a simple crack growth algorithm, as outlined in Fig. 1d, to generate the training and testing datasets for brittle fracture, where we assume that the location of the nearest void to the crack-tip governs the crack growth direction. As depicted in Fig. 1e-i and -ii, the crack propagates diagonal-upwards, straight, or diagonal-downwards (patterned element), depending on whether the nearest void to the crack-tip lies above, on, or below the crack-plane, i.e., regions r_1, r_2, and r_3, respectively, in Fig. 1a-i. When two or more "closest" voids are equidistant to the current crack tip, we then propagate the crack towards the highest porosity regime (r_1, r_2, or r_3) within the process zone, as shown in Figs. 1e-iii and -iv. In the absence of void defects, or in the rare event when the porosities are symmetrical about the crack-plane, we assume the crack propagates straight along r_2 per mode I crack growth. This simple rule-based algorithm allows us to simulate crack growth element-by-element, to obtain the crack path as a function of void heterogeneity in the material. Voids outside of this crack path remain unchanged, which allows for a crack growth response that resembles the infinitesimal damage zone in brittle media.

The brittle crack growth algorithm requires a predefined process zone size, which is material dependent. For each of the five process zone sizes – 3×3, 5×5, 7×7, 9×9, 11×11 grids –

in this study, we generate 50 material samples with random distributions of porosities to produce the dataset for 50 individual cracks of 981 elements in length. Half of the samples have average porosities of 15%, while the remaining half have average porosities of 5%. We intentionally introduce such high porosity levels to enrich the training datasets of our ANN, since the absence of voids within the process zone would result in straight cracks under the proposed crack growth algorithm. Together, these 50 crack samples provide a total of 49,050 observation data, relating void distributions within the process zone (represented by the array in Fig. 1a-i) to the stepwise crack propagation direction (represented by arrays in Fig. 1a-ii). We divide this dataset into training (29,430), validation (9,810) and testing (9,810) data in a 3:1:1 ratio, which are used to calibrate the weights and biases, tune the hyperparameters, and evaluate the predictive accuracy of the ANN.

2.2 Hyperparameter testing

We perform hyperparameter testing to ascertain the optimal ANN architecture (number of hidden layers, nodes per hidden layer) for brittle crack path prediction. For each $n \times n$ process zone size, we train 10 separate ANNs, each with randomly initialized weights, using the training dataset. For each of these 10 ANNs, we use the validation dataset to compute the classification accuracy, defined as the percentage of correct observations. We select the ANN with the highest validation accuracy, and summarize the classification accuracies based on the testing dataset for varying ANN architectures and process zone sizes in Table S1 of the Supplementary Materials. For simplicity, we assume each hidden layer in the ANN architecture has equal number of nodes. Results show that the highest classification accuracies were consistently achieved using a neural network architecture with only one hidden layer. Herein, we will adopt the simplest ANN architecture resulting in the highest testing accuracy (bold) for each process zone size to predict the crack path.

Although the classification accuracies in Table S1 of the Supplementary Materials tend to decrease with increasing grid (process zone) size, these accuracies are still consistently above 98% suggesting that the ANN correctly captures the rule-based crack growth mechanisms in Fig. 1d. Nevertheless, achieving such high classification accuracy requires a priori knowledge of the process zone size, as shown in Table 1. Underestimating or overestimating the process zone size dramatically reduces the predictive accuracies by as much as 50% (off-diagonal entries in Table 1), particularly for larger process zone sizes due to the more complex crack growth algorithms that the ANN has to learn. Since the highest accuracies are consistently obtained for ANN input grid size corresponding to the actual process zone size (diagonal entries in Table 1), we can therefore infer the process zone size numerically from hyperparameter testing, which reflects the ability of the trained neural network to provide physical insights into the process zone characteristics.

2.3 Crack path prediction

We use the optimal ANN architectures trained on datasets for stepwise crack growth above to predict full crack paths. Figures 2 and 3 depict four randomly generated instantiations of void defect distributions (grey elements), with average porosities of 5% and 15%, respectively. We include both the crack paths (black lines) described by our rule-based crack growth algorithm (Fig. 1c) as well as the crack paths predicted by our ANN (red lines), using the same crack initiation location.

Results show that the crack paths predicted by our ANN for both porosity levels are generally in very good agreement with the actual paths determined by our rule-based algorithm. This is despite the much higher average porosities of these samples versus those in typical brittle materials. For the 5% porosity sample in Fig. 2a, no deviation in the crack path was observed across the entire crack propagation length of 986 elements. In two out of three of the remaining samples in Fig. 2, the predicted crack paths were able to reconnect back to the actual crack paths soon after initial deviation (arrows) – this deviation and rapid reconnection was observed multiple times throughout the crack growth process. Similar observations can be found for the 15% porosity samples in Fig. 3. However, the initial deviations of the crack paths for these higher porosity samples typically occur much earlier, with longer detachment lengths along the crack path. This lower predictive performance for higher porosity samples can be attributed to the more complex porosity distributions within the process zone.

Close-up views of void distributions within the process zones at the initial points of crack path deviation (arrows) show that majority of the ANN prediction errors (all except Fig. 2c) stem from inability to discern the crack propagation path when there are two closest voids to the crack-tip. In three of these samples (Figs. 2b, 2d, 3d), these voids are symmetrically distributed about the crack front and the ANN cannot decide on which void to grow towards, although the crack growth algorithm we implemented calls for cracks to grow straight in these cases. In reality, this is a bifurcation problem with a 50% probability of the crack growing towards either of these voids. Similarly, the ANN struggles when faced with more complex void distributions (Fig. 2c, 3a, 3b) which again reflects the reality where the process of crack advance becomes statistical (Ray, 2018). Nevertheless, the ANN predictions of the crack path are sufficiently accurate in view of the much lower porosity levels ($< 1\%$) of typical brittle materials.

3. Artificial Neural Networks for Ductile Media

In contrast to brittle materials, which fail with limited deformation or distortion, ductile materials undergo substantial plastic deformation prior to fracture and have a much larger process zone. The micromechanisms of crack propagation and the ensuing crack paths are also far more complex, with voids surrounding the crack-tip undergoing substantial deformation during crack growth even though they may not coalesce with the main crack – one cannot easily resolve the crack patterns with a simple rule-based algorithm. In conventional metals and metallic alloys, ductile fracture originates from the nucleation, growth, and coalescence of microscopic voids during plastic deformation, giving rise to a dimpled fracture surface. These microscopic voids nucleate from $\sim 2-12$ μm inclusions and second-phase particles (Stone et al., 1985) at stress levels well below the critical cavitation stress (Tvergaard and Hutchinson, 1992), and are often considered to be pre-existing *background voids* in ductile fracture analyses (Chew et al., 2005, 2007). In additively-manufactured (AM) metals, $\sim 30-60$ μm voids resulting from AM processing defects are randomly distributed within the material sample (Panwisawas et al., 2017; Snow et al., 2020; Muro-Barrios et al., 2022), in addition to the smaller background voids from inclusions and second-phase particles, which creates a dual porosity media. The presence of these AM void defects can induce undulating crack paths in the AM specimen (Foehring et al., 2018; VanSickle et al., 2020). As prior studies have shown, strategic placement of these AM voids can substantially improve the fracture resistance (Cui et al., 2020; Muro-Barrios et al., 2022). Here, we train an ANN on datasets generated from a micromechanical ductile fracture model to predict the crack paths in a dual porosity media, representative of AM metals.

3.1 Micromechanical fracture model

Our ductile fracture model consists of a homogeneous material with a semi-infinite crack loaded remotely by mode I K-field loading under plane strain, small-scale yielding conditions (Fig. 4a). Outside of the designated porous zone, an elastoplastic material response is assumed as defined by the uniaxial true stress (σ)–logarithmic strain (ε) relation

$$\varepsilon = \begin{cases} \frac{\sigma}{E} & \sigma < \sigma_0 \\ \frac{\sigma_0}{E}\left(\frac{\sigma}{\sigma_0}\right)^{\frac{1}{N}} & \sigma \geq \sigma_0 \end{cases} \tag{1}$$

where σ_0 is the initial yield stress, E is the Young's modulus, and N is the strain hardening exponent. Generalization to multiaxial stress states assumes isotropic hardening and a von Mises yield condition. In our simulations, we adopt the material parameters of $\sigma_0/E = 0.004$, $N = 0.05$, as well as a Poisson's ratio of $\nu = 0.3$, representative of magnesium alloys.

We model the designated porous zone ahead of the crack with 17 rows of void-containing cell elements, each row of 117 cell elements (Fig. 4b and 4c). While often termed as the "fracture process zone" in micromechanical studies (Xia and Shih, 1995), we instead use the term "designated porous zone" to distinguish this region from the physical process zone that moves with the growing crack-tip. Each cell element of uniform dimensions $D \times D$ contains a void of initial volume fraction f_0. Two distinct size-scales of voids are introduced in our designated porous zone. Larger-scale voids initialized with a porosity of $f_0 = 0.025$ are used to represent void defects originating from unsintered powder particles in AM metals (Liu & Shin, 2019). As depicted by red elements in Fig. 4c, single isolated void defects can represent "keyhole" defects caused by gas entrapment (Panwisawas et al., 2017), while a cluster of 2 or more of these void defects in close-proximity can depict "lack-of-fusion" defects caused by incomplete melting of AM powder particles (Snow et al., 2020). The remaining voids surrounding these larger-scale void defects are the smaller-scale voids, initialized with a porosity of $f_0 = 0.005$, representing background voids nucleated from inclusions and second-phase particles. The behavior of both these void-containing cell elements are governed by the Gurson flow potential (Gurson, 1977)

$$\mathbf{\Phi} = \left(\frac{\sigma_\mathrm{e}}{\bar{\sigma}}\right)^2 + 2q_1 f \cosh\left(\frac{3q_2\sigma_\mathrm{m}}{2\bar{\sigma}}\right) - (1 + (q_1 f)^2) = 0 \tag{2}$$

where σ_{e} is the macroscopic (Mises) equivalent stress, $\bar{\sigma}$ the (Mises) equivalent stress of the matrix material surrounding the phenomenological void, σ_{m} the mean stress, and f the current void volume fraction. The parameters q_1 and q_2 are adjustment parameters introduced to improve predictions for periodic arrays of void-containing computational cells (Tvergaard, 1989), and are taken to be 1.48 and 1.013, respectively (Faleskog et al., 1998). Note that (2) reduces to (1) when $f = 0$. The void growth rate obeys the volumetric plastic strain rate relation

$$\dot{f} = (1 - f)\mathrm{tr}\mathbf{d}^{\mathrm{p}} \tag{3}$$

where $\mathrm{tr}\mathbf{d}^{\mathrm{p}}$ is the trace of the plastic deformation rate $\mathbf{d}^{\mathrm{p}}$. Together, (2) and (3) govern the void growth process.

Our finite element analyses are performed using the open-source 3D finite element code WARP3D (Koppenhoefer et al., 1994). Our finite element mesh comprises of an (x_1, x_2)-plane of 7,096 linear, 8-noded brick elements of uniform thickness *D* along the x_3-axis, with out-of-plane displacements $u_3 = 0$ imposed for all nodes resulting in plane strain boundary conditions. Along the remote circular boundary of the finite element mesh (Fig. 4c), we impose the elastic asymptotic in-plane displacement fields

$$\begin{aligned} u_1(R,\theta) &= K_{\mathrm{I}}\frac{1+\nu}{E}\sqrt{\frac{R}{2\pi}}(3-4\nu-\cos\theta)\cos\frac{\theta}{2} \\ u_2(R,\theta) &= K_{\mathrm{I}}\frac{1+\nu}{E}\sqrt{\frac{R}{2\pi}}(3-4\nu-\cos\theta)\sin\frac{\theta}{2} \end{aligned} \tag{4}$$

where $R = \sqrt{x_1^2 + x_2^2}$ and $\theta = \tan^{-1}\frac{x_2}{x_1}$ for nodes on the remote boundary. For the crack geometry in this study, the energy release rate or *J*-integral is related to the mode I stress intensity factor K_{I} by

$$J = \frac{1-\nu^2}{E}K_{\mathrm{I}}^2 \tag{5}$$

To verify that small-scale yielding condition is satisfied, we compute the *J*-integral on several contours around the crack using domain integral method at various loading stages (Moran and Shih, 1987). The domain integral values are in good agreement with the *J*-integral value in (5) for the prescribed K_I value.

3.2 Crack growth datasets

Crack propagation simulations are performed using an element extinction procedure in WARP3D, where cell elements within the process zone are deleted when the porosity reaches a critical value of $f_c = 0.2$. We consider elements with $f \geq 0.15$ to constitute the crack – the cell with the average void volume fraction, $f_\mathrm{tip} = 0.15$, is taken as the effective location of the crack-tip. Under these conditions of crack advance, the crack growth resistance Γ equates with the *J*-integral value in (5). Here, we train our ANN on datasets generated from stepwise crack growth simulations, and utilize the calibrated neural network to achieve full crack path predictions from given distributions of void defects in the designated porous zone of the material samples. The adopted ANN architecture is similar to Fig. 1b, but with five possible outputs, representing stepwise crack propagation directions labeled $1-5$ in Fig. 4c. The training dataset comprises of detailed crack-void interaction studies to elucidate how the dual-scale configuration of voids ahead of a crack can induce adjacent elements to the current crack-tip (labeled $1-5$ in Fig. 4c) to reach f_tip, and in turn, f_c, to initiate void coalescence and subsequent crack advance. We introduce 1 to 4 nucleation sites for void defects (larger-scale voids) to form within $6D \leq x_1 \leq 15D$ of the designated porous zone, with a biased probability towards $x_1 = 6D$; each nucleation site in turn has nearly equal probability of forming 1 to 4 void defects in close proximity, which can result in either the formation of smaller keyhole defects represented by a single, isolated void defect, or the formation of larger, elongated lack-of-fusion defects represented by a cluster of 2 to 4 void defects in close-proximity. We propagate the crack under K_{I} loading and track the propagation directions (1 to 5) of the crack as the crack length increases from $\Delta a = 4D$ to $5D$, and subsequently, $\Delta a = 5D$ to $6D$. Thus, each simulation run provides two pairs of input-output datasets, relating the *initial* porosity distribution ahead of the current crack-tip to the stepwise crack propagation direction. In all cases, we initiate crack propagation from the notch-tip centered at $x_1 = x_2 = 0$, but we only record the crack growth data beyond $\Delta a \geq 4D$ to avoid notch-tip effects.

Through the above procedure, we obtain a total of 14,427 observations: 970 (class 1), 1521 (class 2), 9,684 (class 3), 1,370 (class 4), and 882 (class 5) samples, each class corresponding to the crack propagation direction labeled $1-5$ in Fig. 4c. A dataset with an imbalance in the quantity of observations for each output class often leads to inferior predictive capability compared to one with a balanced dataset (Mazurowski et al., 2008). In the case of our crack growth simulations, an overly unbalanced dataset comprising of mostly class 3 (straight crack growth) members can lead to spurious results, where high accuracies in predicting straight cracks and poor accuracies in predicting undulating cracks can still result in a perceived high overall classification accuracy. Studies have shown that an imbalance ratio, defined by proportion of samples in the majority to minority class, of below 10 only causes a modest reduction in classification accuracy (Prati et al., 2015). Since our crack growth dataset is generated under mode I loading, the majority of our cracks tend to grow straight (class 3), resulting in an imbalance ratio of 11. Accordingly, we randomly remove samples to reduce the class 3 dataset to 3,068 samples, and achieve an imbalance ratio of 3.5. We use this balanced dataset to quantify the size of the process zone below.

3.3 Hyperparameter testing

The process zone size for crack-void interactions can be iteratively determined, by varying the columns of void-containing computational cell elements both ahead of (n^+) and behind the current crack-tip (n^-) used in our ANN input, and quantifying the corresponding testing accuracies of the ANN. Instead, we will quantify the process zone size by examining the weights of the neural network after training. We start with a conservative estimate of the process zone size, encompassing computational cell elements between the limits of $n^- = 4$ and $n^+ = 11$. Per our previous analyses in Section 2, elements representing void defects and background voids within the process zone are labeled '1' and '0' in the ANN input respectively. Since the process zone now encompasses columns of elements behind the current crack-tip, cracked elements (defined as those with void porosities exceeding f_{tip}) are now labeled '-1' in the ANN input, which allows the neural network to account for the effects of crack profile on the crack growth direction. We conduct a ten-fold cross validation analysis, by dividing the entire balanced dataset for stepwise crack growth into 10 subsets (folds): 9 of these subsets are used to train an ANN, while the remaining subset is used to validate the accuracy of the ANN. We repeat this process for over 10 iterations using a different subset for validation at each iteration, and obtain the final validation accuracy by averaging the classification accuracies over all iterations.

As shown in Table S2 of the Supplementary Materials, the validation accuracies are generally not sensitive to the number of hidden layers or nodes, and an ANN with a single hidden layer of 100 hidden nodes is optimal for predicting ductile crack growth. Using this architecture, we compute the two-norm of all weights used to connect input node j of the neural network to the single hidden layer

$$I_j = \sqrt{\textstyle\sum_{i=1}^{n} w_{ij}^2} \tag{6}$$

where w_{ij} is the weight connecting the input node j to the hidden layer node i, and n is the number of nodes in the hidden layer. A larger I_j value infers that the input node j has larger influence over the output, and quantitatively provides the physical relationship for crack-void interactions, i.e., between the spatial location of voids with respect to the current crack-tip, and its influence on the crack propagation direction. Figure 5a summarizes the I_j values corresponding to elements representing the input nodes to the ANN. Observe that highest I_j value resides directly ahead of the current crack-tip, and the I_j distribution generally follows the butterfly-shaped plastic region ahead of the crack-tip as shown in Fig. 5b. From inspect of both these two-norm values and plastic strain contours, we conclude that selection of $n^+ = 8$ as the right boundary of the process zone would encompass all elements ahead of the crack undergoing significant plastic deformation (correlates with $I_j \geq 3.5$). Elevated I_j values behind the crack-tip are observed for elements adjacent to the current crack-tip (yellow) spanning $n^- \leq 2$, and are related to the influence of the crack profile on crack growth direction. Outside of this regime, I_j values are low since void defects are absent aft of the crack-tip in our training datasets – we do not expect void defects behind the crack-tip to influence crack advance, and will artificially remove these defects in our ANN inputs for predictions of the full crack profiles detailed later. Our numerical studies show that fixing the right boundary of the process zone at $n^+ = 8$, while shifting the left boundary from $n^- = 2$ to 1 results in a marginal loss of validation accuracy from 89.9% to 89.7%. Herein, our ANN inputs for ductile crack growth will encompass cell elements within the limits of $n^- = 1$ and $n^+ = 8$ (green dashed lines in Fig. 5a).

Using the newly established process zone size, as informed by our ANN, we repeat our hyperparameter studies and achieve a validation accuracy of 90.0% with an optimal ANN comprising of a single hidden layer with 110 hidden nodes. With this architecture, we rebalance our training dataset, by starting again with the full class 3 dataset of 9,684 samples, and randomly removing class 3 samples to reduce the imbalance ratio. We find that a class 3 dataset of 4,410 samples, resulting in an imbalance ratio of 5, provides an optimal balance for predictive accuracies across all 5 classes. Table 2 shows the confusion matrix, detailing the relationship between the actual versus predicted output classes. Observe that our ANN correctly predicts the stepwise crack propagation direction with accuracies ranging from ~81-92%. While seemingly low compared to our brittle crack growth predictions in Section 2, the majority of errors stems from confusion between neighboring classes. These are relatively minor errors since the cracks still propagate in the same general directions for these cases.

3.4 Crack path predictions

We validate the accuracy of the calibrated ANN in predicting the full crack paths in samples with spatially varying distributions of void defects, generated through a similar process outlined in Section 3.2 for the training datasets. A total of 1 to 4 nucleation sites are introduced within the designated porous zone in our small-scale yielding model. Each nucleation site in turn contains a single isolated void defect (keyhole) or a cluster of void defects in close proximity (lack-of-fusion). We classify samples with only 1 or 2 nucleation sites as having low defect densities, and samples with 3 or 4 nucleation sites as having high defect densities. Figures 6 and 7 show the porosity distributions and associated crack paths along samples with low and high defect densities, with different instantiations of void defect distributions highlighted in red. Even when the cracks are undulating, ANN predictions of the crack paths, denoted by cyan symbols, are in near perfect agreement with the actual crack paths simulated by our micromechanics-based model for both low and high defect density samples.

We note that the void defects are well-dispersed within the samples in Figs. 6 and 7. When there are either vertical clusters of voids or multiple single/connected voids in close proximity, there is less certainty in the ANN predictions, which can result in deviations of the crack path from the micromechanical model. Figure 8 highlights four of such cases, where we number sequentially (cyan) the crack propagation path predicted by the ANN. We also include the ANN output vectors corresponding to the first 10 crack propagation steps, i.e. up to $\Delta a = 10D$, in Table S3 of the Supplementary Materials. The ANN output vector at each step indicates the probabilities for crack growth in each of the five possible directions, and we consistently observe lower confidence in the ANN predictions at the point of deviation from the actual crack path. This uncertainty in crack path predictions can reflect reality, since the exact location of void defect coalescence with the propagating crack may be sensitive to extraneous factors, such as the magnitude of K_{I} loading, current deformation states of the void defects, etc., which our training dataset do not account for.

In our earlier crack growth predictions, we assign the crack path to follow the crack growth direction with the highest probability predicted by our ANN. However, the probabilistic output of this neural network architecture also enables us to represent stochastic crack growth via a variety of possible crack paths with relative likelihood assigned to each one. To this end, we generate multiple possible crack paths through a Monte Carlo approach by assigning the crack growth direction at each crack growth instant ($\Delta a/D$) based on the outcome of random draws from the probability distribution of the five possible directions provided by the ANN output vector. We quantify the likelihood of each of these possible crack paths through the combined probability along each path.

Figure 9 shows three examples of stochastic crack growth for three instantiations of void defect distributions, along with the probability of the selected crack growth direction at each $\Delta a/D$. In the presence of a single void defect located $3D$ away from the initial crack front (Fig. 9a), our ANN predicts a straight crack path (red symbols) as the most probable outcome with a high likelihood of 97.6%. Additionally, our ANN predicts a crack path which coalesces with the defect site (green symbols) as a possible, but improbable crack path with a likelihood of 1.1%. Thus, this specific case reflects a near-deterministic crack path prediction by the neural network. In the presence of two proximate void defects in Fig. 9b, however, the crack path is no longer deterministic. The dominant crack path (red symbols) propagates through the closest void defect and has a likelihood of 49.9%. However, the alternative crack path (green symbols) which coalescences with the second void defect has a non-negligible likelihood of 31.3%. This reflects the increasing stochasticity of crack growth with increasing number of void defects in close proximity. This stochastic nature of crack growth is further exacerbated in the presence of multiple void clusters in Fig. 9c, where we observe an almost equal likelihood of 22.2% and 19.2% for crack propagation along distinctly different paths denoted by red and green symbols, respectively, which potentially leads to crack branching. The exact point of deviation of these two pathways can vary, and we show in blue symbols a third possible crack path with a likelihood of 4.8%. For all three cases in Fig. 9, the crack paths from our micromechanical model are in exact agreement with the highest likelihood crack paths predicted by our ANN (red symbols). This ability of our ANN architecture to learn to provide a multiplicity of possible crack paths demonstrates the value of a statistical-based neural network model over traditional deterministic micromechanical fracture models.

Studies have demonstrated two distinct mechanisms for ductile fracture (Tvergaard and Hutchinson, 2002): (**a**) void-by-void coalescence with the main crack where the crack grows sequentially, or (**b**) multiple void interaction leading to the formation of unconnected damage zone(s) ahead of the crack-tip which eventually coalesce to advance the crack. Since our training data is based on stepwise crack growth, a sequential void-by-void crack advance is inherently assumed in our ANN. Hence, the exact crack propagation sequence by our ANN may not reflect reality when multiple void interaction is active. Nevertheless, our ANN appears capable of capturing the *overall* crack profiles even with the formation of unconnected damage zones (Figs. 6 and 7), with the exception of one scenario involving the presence of a void defect/cluster proximate to these isolated damage zones. We depict the crack growth sequence for two such cases in Fig. 10, where an unconnected damage zone, centered on a diagonal void defect, develops ahead of the current crack-tip. This unconnected damage zone extends horizontally across several elements prior to coalescence with the main crack, which prevents interaction or coalescence with nearby void defects. Because our ANN assumes sequential crack growth, it fails to account for the horizontal extended damage zone, and the predicted crack path instead spans between these void defects (magenta symbols).

We remark that the presence of an isolated void defect near a propagating crack generally results in the formation of an isolated, extended damage zone. This damage zone centers on the pre-existing void defect, and extends horizontally through multiple elements ($\sim 3-5D$) prior to coalescence with the main crack (step 85 in Fig. 10a, step 67 in Fig. 10b). Heuristically, one can anticipate the formation of this extended damage zone by adding three horizontal void defects to form this extended damage zone just prior to coalescence of the pre-existing void defect with the main crack. We augment our ANN to include this simple criterion, with exception when there are pre-existing voids located along or adjacent to this "extended" damage zone, which may influence the crack path. With this augmentation, our predicted crack paths (cyan symbols in Fig. 10) are now in perfect agreement with the micromechanical models.

4. Crack Path Design

For the ductile fracture analyses, simulating the full crack paths with FEM required, on average, 27.06 s of wall time, while each ANN prediction of the crack path took an average of 1.32 s of wall time. This ability to rapidly predict the crack path from given initial void defect distributions through an ANN provides the basis to achieve crack path design. In this section, we adopt an evolutionary genetic algorithm (GA), outlined in Fig. 11a, to optimize the spatial distribution of void defects to achieve a set of predefined crack paths in brittle and ductile media. The GA is first initialized by generating a population of size n_p, each member comprising of a grid of elements encompassing the targeted crack profile. A proportion of r elements are set to '1' to denote the void defects, while the remainder are set to '0' to denote the background material. In each iteration of the GA, we randomly pair up members of the population as parents. Each pair of parents in turn creates two offspring via uniform crossover to generate an additional n_p members, increasing the total population size to $2n_p$. A mutation step is performed among the offspring members by randomly selecting μ proportion of elements per member whose binary values are to be flipped. For each member of the population, we predict the crack path from the distribution of void defects with our ANNs. We compute the cost function for each member of the population

$$C = \frac{1}{L}\sqrt{\sum_{i=1}^{L}\left(y_i^p - y_i^t\right)^2} + \rho n_v \tag{7}$$

where L is the number of elements spanning the horizontal crack length, y_i^p and y_i^t are the vertical positions of the predicted and targeted crack elements along the i^{th} column of the grid (mean values are used for vertical cracks), ρ is the weighting factor, and n_v is the proportion of elements containing void defects. A higher value of ρ creates a preference for minimizing the number of void defects, but at the expense of accuracy between the targeted and predicted crack paths. We keep the top n_p members with the lowest cost function, and repeat the entire process until the member with the lowest cost function in (7) converges to below a set criteria (0.01 for brittle media, 0.1 for ductile media), or when the maximum number of iterations (~200–1000) has been reached. Table 3 summarizes the parameters used in the GA for brittle and ductile media.

We show in Fig. 11b the evolution of the cost function with number of iterations in the GA for a brittle media, and include snapshots of the void defect placement (red elements) in relation to the predicted (cyan symbols) and targeted (magenta symbols) crack paths during the optimization process. The initial rapid and monotonic decrease of the cost function coincides with the increasing alignment between the predicted and targeted crack paths. Subsequent gradual decrease in cost function (with the use of a low ρ) is associated with the removal of extraneous void defects that have limited influence on the crack path. Figure 11c shows the optimized porosity distributions for three other brittle crack designs; we also include the actual crack path governed by our rule-based brittle crack growth algorithm (black cells), confirming that we have indeed obtained the desired crack paths with these optimized defect locations.

In the case of ductile fracture, the strategic placement of void defects can significantly influence the fracture toughness. Figures 12a and 12b depict two void defect instantiations (red elements), resulting in $\sim 50\%$ and $\sim 30\%$ improvements in the steady-state fracture toughness (solid lines) versus the baseline material containing no void defects (dashed lines). The ANN is able to accurately predict the crack paths (cyan symbols) for both these void defect instantiations. To determine if controlling the crack path alone is sufficient to guarantee a desired fracture resistance response, we set the predicted crack paths in Fig. 12 (cyan symbols) as the targeted crack paths in our GA to obtain the “optimized” void defect distributions in Fig. 13 (red elements) to achieve these pathways. Based on these optimized void defect locations, we determine the actual crack paths from our micromechanics model, which are in relatively good agreement with both the ANN-predicted (cyan symbols) and targeted crack paths (magenta symbols). Surprisingly, the associated fracture toughness values between Figs. 12a versus 13a, as well as Figs. 12b versus 13b, are very different despite the similarities in the crack patterns – the steady-state toughness is only slightly higher than the baseline case for Fig. 13a, while no improvements in the fracture toughness is observed for Fig. 13b. Thus, two different initial porosity distributions can lead to the same final crack patterns, while possessing very different fracture resistance. We attribute this to the differing void growth mechanisms associated with these porosity distributions. In the case of Figs. 12a and 12b, an isolated damage zone centered on the off-diagonal void cluster to the main crack path develops early during crack propagation, which results in the rapid increase in the fracture resistance at small crack lengths ($\Delta a \sim 5D$). While isolated damage zones similarly develop for the void placements in Figs. 13a and 13b, the more dispersed void defects result in the formation of multiple but smaller damage zones that coalesce with the main crack at much lower loadings.

5. Concluding Remarks

In the modeling of AM metals, the strategic placement of AM voids within the material was found to control the crack path and resulting fracture resistance, lending possibility to crack path design through optimized void placement in the material (Yue et al., 2020; Muro-Barrios et al., 2022). In this work, we have demonstrated that such concepts are achievable with ANNs for machine learning. Utilizing datasets generated from a simple rule-based algorithm for brittle materials, as well as more complex micromechanical ductile fracture models, we have shown that the ANNs are capable of accurately predicting undulating crack paths in both brittle and ductile heterogeneous media even at high defect densities. We were also able to quantify the size of the fracture process zone through hyperparameter testing of the ANNs. By implementing these ANNs in a GA framework, we have successfully optimized the void defect distributions to achieve a sampling of targeted crack paths, bringing us a step closer to achieving “fracture-by-design”.

Errors in our ANN predictions primarily arise from two sources: (**a**) complex crack-void interactions involving vertical cluster of void defects or multiple void defects/clusters in close proximity to the propagating crack-tip, and (**b**) differing mechanisms of crack growth. The former results in a multiplicity of possible crack paths, which reflects the statistical nature of fracture. We demonstrate that one of the key advantages of the neural network architecture over traditional deterministic fracture models is in the ability of the ANN to predict a multiplicity of possible crack paths, along with a quantified likelihood of each path. The latter is a fundamental issue in ductile fracture, where the mechanisms of void-by-void growth versus multiple void interaction depend on specific void defect arrangements. Since our training dataset assumes sequential void-by-void crack growth, our ANN cannot correctly resolve the exact void growth sequence leading to the formation of multiple damaged zones ahead of the crack-tip, even though the ANN-predicted crack profiles are still accurate. Nevertheless, distinguishing between these mechanisms is important in crack path design, since two differing initial porosity distributions resulting in the same crack path can exhibit distinctly different fracture toughness response.

Acknowledgement

The authors acknowledge the support provided by National Science Foundation under Grant No. NSF-CMMI-2009684.

References

Abuzaid, W., Oral, A., Sehitoglu, H., Lambros, J., Maier, H.J., 2013. Fatigue crack initiation in Hastelloy X – The role of boundaries. Fatigue Frac. Eng. Mater. Struct. 36, 809-826.

Adda-Bedia, M., 2005. Brittle fracture dynamics with arbitrary paths. III. The branching instability under general loading. J. Mech. Phys. Solids 53, 227-248.

Buehler, M.J., 2022. Modeling atomistic dynamic fracture mechanisms using a progressive transformer diffusion model. Journal of Applied Mechanics, 89(12), doi:10.1115/1.4055730.

Chan, K.S., 2009. Roles of microstructure in fatigue crack initiation. Int. J. Fatigue 32, 1428.

Chew, H.B., 2014. Cohesive zone laws for fatigue crack growth: Numerical field projection of the micromechanical damage process in an elasto-plastic medium. Int. J. Solids Struct. 51, 1410-1420.

Chew, H.B., Guo, T.F., Cheng, L., 2005. Vapor pressure and residual stress effects on failure of an adhesive film. Int. J. Solids Struct. 42, 4795-4810.

Chew, H.B., Guo, T.F., Cheng, L., 2007. Pressure-sensitive ductile layers –I. Modeling the growth of extensive damage. Int. J. Solids Struct. 44, 2553-2570.

Chew, H.B., Hong, S., Kim, K.-S., 2009. Cohesive zone laws for void growth—II. Numerical field projection of elasto-plastic fracture processes with vapor pressure. J. Mech. Phys. Solids 57, 1374-1390.

Cotterell, B., Rice, J.R., 1980. Slightly curved or kinked cracks. Int. J. Fract. 16, 155-169.

Cui, Y., Chew, H.B., 2022. Machine-learning prediction of atomistic stress along grain boundaries. Acta Mater. 222, 117387.

Cui, Y., Gao, Y.F., Chew, H.B., 2020. Two-scale porosity effects on cohesive crack growth in a ductile media. Int. J. Solids Struct. 200, 188-197.

Erdogan, F., Sih, G.C., 1963. On the crack extension in plates under plane loading and transverse shear. ASME J. Basic Eng. 85, 519-525.

Faleskog, J., Shih, C.F., 1997. Micromechanics of coalescence—I. Synergistic effects of elasticity, plastic yielding and multi-size-scale voids. J. Mech. Phys. Solids 45, 21-25, 27-50.

Fleck, N.A., Hutchinson, J.W., Suo, Z., 1991. Crack path selection in a brittle adhesive layer. Int. J. Solids Struct. 27, 1683-1703.

Foehring, D., Chew, H.B., Lambros, J., 2018. Characterizing the tensile behavior of additively manufactured Ti-6Al-4V using multiscale digital image correlation. Mater. Sci. Eng. A 724, 536-546.

Francfort, G.A., Marigo, J.-J., 1998. Revisiting brittle fracture as an energy minimization problem. J. Mech. Phys. Solids 46, 1319-1342.

Goldstein, R.V., Salganik, R.L., 1974. Brittle fracture of solids with arbitrary crack. Int. J. Fract. 10, 507-523.

Guilloteau, E., Charrue, H., Creuzet, F., 1996. The direct observation of the core region of a propagating fracture crack in glass. Europhysics Lett. 34, 549.

Gurson, A.L., 1977. Continuum theory of ductile rupture by void nucleation and growth: Part I – Yield criteria and flow rules for porous ductile media. Trans. J. Eng. Mater. Tech. 99, 2-15.

Homer, E.R., Hensley, D.M., Rosenbrock, C.W., Nguyen, A.H., Hart, G.L., 2019. Machine-learning informed representations for grain boundary structures. Front. Mater. 6, 168.

Hong, S., Chew, H.B., Kim, K.-S., 2009. Cohesive-zone laws for void growth—I. Experimental field projection of crack-tip crazing in glassy polymers. J. Mech. Phys. Solids 57, 1357-1373.

Hsu, Yu-Chuan, Yu, Chi-Hua, Buehler, M.J., 2020. Using deep learning to predict fracture patterns in crystalline solids. Matter 3, 197–211.

Huber, L., Hadian, R., Grabowski, B., Neugebauer, J., 2018. A machine learning approach to model solute grain boundary segregation. NPJ Comput. Mater. 4, 1-8.

Hunter, A., Moore, B.A., Mudunuru, M., Chau, V., Tchoua, R., Nyshadham, C., Karra, S., O'Malley, D., Rougier, E., Viswanathan, H., Srinivasan, G., 2019. Reduced-order modeling through machine learning and graph-theoretic approaches for brittle fracture applications. Comput. Mater. Sci. 157, 87-98.

Hutchinson, J.W., Evans, A.G., 2000. Mechanics of materials: top-down approaches to fracture. Acta Mater. 48, 125-135.

Kim, S.W., Chew, H.B., Kumar, K.S., 2013. In situ TEM study of crack–grain boundary interactions in thin copper foils. Scripta Mater. 68, 154-157.

Koppenhoefer, K.C., Gullerud, A.S., Ruggieri, C., Dodds, R.H. Jr., Healey, B.E., 1994. WARP3D: Dynamic nonlinear analysis of solids using a preconditioned conjugate gradient software architecture. IDEALS (illinois.edu). https://www.ideals.illinois.edu/handle/2142/14220.

Lew, A.J., Buehler, M.J., 2021. A deep learning augmented genetic algorithm approach to polycrystalline 2D material fracture discovery and design. Applied Physics Reviews 8, 041414.

Li, R., Chew, H.B., 2017. Grain boundary traction signatures: Quantifying the asymmetrical dislocation emission processes under tension and compression. J. Mech. Phys. Solids 103, 142-154.

Liu, S., Shin, Y.C., 2019. Additive manufacturing of Ti6Al4V alloy: A review. Mater. Des. 164, 107552.

Mazurowski, M.A., Habas, P.A., Zurada, J.M., Lo, J.Y., Baker, J.A., Tourassi, G.D., 2008. Training neural network classifiers for medical decision making: The effects of imbalanced datasets on classification performance. Neural Netw. 21(2), 427–436.

McVeigh, C., Vernerey, F., Liu, W.K., Moran, B., Olson, G., 2007. An interactive micro-void shear localization mechanism in high strength steels. J. Mech. Phys. Solids 55, 225-244.

Miehe, C., Teichtmeister, S., Aldakheel, F., 2016. Phase-field modelling of ductile fracture: A variational gradient-extended plasticity-damage theory and its micromorphic regularization. Phil. Trans. Roy. Soc. A 374, 20150170.

Moore, B.A., Rougier, E., O'Malley, D., Srinivasan, G., Hunter, A., Viswanathan, H., 2018. Predictive modeling of dynamic fracture growth in brittle materials with machine learning. Comput. Mater. Sci. 148, 46-53.

Moran, B., Shih, C.F., 1987. A general treatment of crack tip contour integrals. Int. J. Fract. 35, 363-371.

Mozaffar, M., Bostanabad, R., Chen, W., Ehmann, K., Cao, J., Bessa, M. A., 2019. Deep learning predicts path-dependent plasticity. Proc. Natl. Acad. Sci. 116, 26414-26420.

Murali, P., Guo, T.F., Zhang, Y.W., Narasimhan, R., Li, Y., Gao, H.J., 2011. Atomic scale fluctuations govern brittle fracture and cavitation behavior in metallic glasses. Phys. Rev. Lett. 107, 215501, 2011.

Muralidharan, K., Simmons, J.H., Deymier, P.A., Runge, K., 2005. Molecular dynamics studies of brittle fracture in vitreous silica: Review and recent progress. J. Non-Crystalline Solids 351, 1532–1542.

Muro-Barrios, R., Cui, Y., Lambros, J., Chew, H.B., 2022. Dual-scale porosity effects on crack growth in additively manufactured metals: 3D ductile fracture models. J. Mech. Phys. Solids 159, 104727.

Panwisawas, C., Perumal, B., Ward, R.M., Turner, N., Turner, R.P., Brooks, J.W., Basoalto, H.C., 2017. Keyhole formation and thermal fluid flow-induced porosity during laser fusion welding in titanium alloys: experimental and modelling. Acta Mater. 126, 251-263.

Pierson, K., Rahman, A., Spear, A.D., 2019. Predicting microstructure-sensitive fatigue-crack path in 3D using a machine learning framework. JOM 71, 2680-2694.

Prakash, D.G.L, Walsh, M.J., Maclachlan, D., Korsunsky, A.M., 2009. Crack growth micro-mechanisms in the IN718 alloy under the combined influence of fatigue, creep and oxidation. Int. J. Fatigue 31, 1966-1977.

Prati, R.C., Batista, G.E.A.P.A., Silva, D.F., 2015. Class imbalance revisited: A new experimental setup to assess the performance of treatment methods. Knowl. Inf. Syst. 45, 247–270.

Ray, P., 2018. Statistical physics perspective of fracture in brittle and quasi-brittle materials. Phil. Trans. R. Soc. A 377, 20170396.

Rovinelli, A., Sangid, M.D., Proudhon, H., Ludwig, W., 2018. Using machine learning and a data-driven approach to identify the small fatigue crack driving force in polycrystalline materials. NPJ Comput. Mater. 4, 35.

Rozen-Levy, L., Kolinski, J.M., Cohen, G., Fineberg, J., 2020. How fast cracks in brittle solids choose their path. Phy. Rev. Lett. 125, 175501.

Sargado, J.M., Keilegavlen, E., Berre, I., Nordbotten, J.M., 2018. High-accuracy phase-field models for brittle fracture based on a new family of degradation functions. J. Mech. Phys. Solids 111, 458-489.

Slepyan, L.I., 1993. Principle of maximum energy dissipation rate in crack dynamics. J. Mech. Phys. Solids 41, 1019-1033.

Snow, Z., Nassar, A.R., Reutzel, E.W., 2020. Invited review article: review of the formation and impact of flaws in powder bed fusion additive manufacturing. Addit. Manuf. 36, 101457.

Stone, R.H.V., Cox, T.B., Low, J.R., Psioda, J.A., 1985. Microstructural aspects of fracture by dimpled rupture. Int. Met. Rev. 30, 157-180.

Tanné, E., Li, T., Bourdin, B., Marigo, J.-J., Maurini, C., 2018. Crack nucleation in variational phase-field models of brittle fracture. J. Mech. Phys. Solids 110, 80-99.

Tekoglu, C., Hutchinson, J.W., Pardoen, T., 2015. On localization and void coalescence as a precursor to ductile fracture. Phil. Trans. R. Soc. A., 373, 20140121.

Tran, H., Gao, Y.F., Chew, H.B., 2022. An inverse method to reconstruct crack-tip cohesive zone laws for fatigue by numerical field projection. Int. J. Solids Struct. 239, 111435.

Tran, H., Chew, H.B., 2022. Cohesive zone interpretations of phase-field fracture models. J. Appl. Mech. 89, 121005.

Tvergaard, V., 1989. Material failure by void growth to coalescence. Adv. Appl. Mech. 27, 83-151.

Tvergaard, V., Hutchinson, J.W., 1992. The relation between crack growth resistance and fracture process parameters in elastic-plastic solids. J. Mech. Phys. Solids 40, 1377-1397.

Tvergaard, V., Hutchinson, J.W., 2002. Two mechanisms of ductile fracture: Void by void growth versus multiple void interaction. Int. J. Solids Struct. 39, 3581–3597.

VanSickle, R., Foehring, D., Chew, H.B., Lambros, J., 2020. Microstructure effects on fatigue crack growth in additively manufactured Ti–6Al–4V. Mater. Sci. Eng. A795, 139993.

Van Brutzel, L., Rountree, C.L., Kalia, R.K., Nakano, A., Vashishta, P., 2002. Dynamic fracture mechanisms in nanostructured and amorphous silica glasses million-atom molecular dynamics simulations. Mater. Res. Soc. Symp. Proc. 703, 117–122.

Wang, H., Zhang, W., Sun, F., Zhang, W., 2017. A comparison study of machine learning based algorithms for fatigue crack growth calculation. Materials 10, 543.

Wang, Y., Oyen, D., Guo, W., Mehta, A., Scott, C.B., Panda, N., Fernandez-Godino, M.G., Srinivasan, G., Yue, X., 2021. Deep learning to predict stress with fracture propagation in brittle materials. NPJ Mater. Degrad. 5, 6.

Williams, J.G., Hadavinia, H., 2002. Analytical solutions for cohesive zone models. J. Mech. Phys. Solids 50, 809-825.

Wu, C.H., 1978. Fracture under combined loads by maximum-energy-release rate criterion. J. Appl. Mech. 45, 553-558.

Wu, J., 2017. A unified phase-field theory for the mechanics of damage and quasi-brittle failure. J. Mech. Phys. Solids 103, 72-99.

Xia, L., Shih, C.F., 1995. Ductile crack growth – I. A numerical study using computational cells with microstructurally-based length-scales. J. Mech. Phys. Solids 43, 233-259.

Xie, D., Zhang, W., Lyu, Z., Liaw, P.K., Tran, H., Chew, H.B., Wei, Y., Ren, Y., Gao, Y., 2022. Plastic anisotropy and twin distributions near the fatigue crack tip of textured Mg alloys from in situ synchrotron x-ray diffraction measurements and multiscale mechanics modeling. J. Mech. Phys. Solids 165, 104936.

Zhu, Q., Samanta, A., Li, B., Rudd, R. E., Frolov, T., 2018. Predicting phase behavior of grain boundaries with evolutionary search and machine learning. Nat. Commun. 9, 467.

Table 1. Testing accuracies (%) for different combinations of input grid and process zone sizes.

		Process Zone Size			
		3×3	5×5	7×7	9×9
Input Grid Size	3×3	100.00	63.32	53.84	48.20
	5×5	83.30	99.86	53.78	48.06
	7×7	82.33	61.76	99.52	46.09
	9×9	81.92	62.24	52.08	98.82
	11×11	78.13	59.43	52.08	44.87

Table 2. Confusion matrix (%) for ANN predictions of crack growth directions in ductile media.

		Predicted Output Class				
		1	2	3	4	5
True Output Class	1	85.24	6.19	7.62	0.48	0.48
	2	3.51	90.54	4.32	1.08	0.54
	3	2.16	1.08	92.34	2.61	1.80
	4	0.29	0.86	5.48	89.34	4.03
	5	0.98	1.46	5.37	11.71	80.49

Table 3. Parameters used in the Genetic Algorithm (GA) for optimization of void defect distributions in brittle and ductile media.

Constant	**Brittle Media**	**Ductile Media**
Population size, n_p	50	50
Initial defect proportion, r	0	0.01
Mutation proportion, μ	0.005	0.005
Horizontal crack length, L (elements)	25	25
Weighting factor, ρ	1	5

Figure Captions

Figure 1: (**A**) Process zone with void defects represented by an $n \times n$ grid of elements (bold solid line region) versus possible crack propagation directions (arrows). (**B**) Artificial neural network (ANN) linking void defect locations within the process zone (input) and the crack propagation direction (output). (**C**) Coalescence of a crack with void defects in additively-manufactured Ti-6Al-4V, resulting in deviation in crack path (VanSickle et al., 2020). (**D**) Flow chart of a rule-based, crack propagation algorithm for brittle fracture. (**E**) Examples of crack propagation direction (patterned element) from given void defect distributions within the process zone.

Figure 2: Comparison of the actual (black) versus ANN-predicted crack paths (red) for four instantiations of void defect distributions (grey pixels) with average porosity of 5%. Void defect configuration within the process zone at first instance of crack path deviation denoted by arrows.

Figure 3: Comparison of the actual (black) versus ANN-predicted crack paths (red) for four instantiations of void defect distributions (grey pixels) with average porosity of 15%. Void defect configuration within the process zone at first instance of crack path deviation denoted by arrows.

Figure 4: (**A**) Boundary layer model with a centerline crack subjected to mode I K-field loading. (**B**) Schematic of dual-scale porosities comprising of void defects and background voids within a designated porous zone modeled by computational cell elements. (**C**) Finite element mesh of the boundary layer model, with close-up view of the crack (black elements); possible crack propagation directions as marked (1–5), with distribution of isolated or clustered void defects (red elements).

Figure 5: (**A**) Contours of two-norm of weights (values as marked) linking elements representing the input nodes to the hidden layer in the ANN. *Yellow element*: current crack-tip; *green boundaries*: final selected process zone. (**B**) Equivalent plastic strain ($\bar{\epsilon}^p$) contours directly ahead of the current crack-tip at three crack lengths (Δa).

Figure 6: ANN-predicted crack paths (cyan symbols) versus actual crack paths (porosity distributions) for different instantiations of low-density void defects (red elements).

Figure 7: ANN-predicted crack paths (cyan symbols) versus actual crack paths (porosity distributions) for different instantiations of high-density void defects (red elements).

Figure 8: Crack growth sequence (cyan) in ANN-predicted crack paths versus actual crack paths (porosity distributions) in the presence of vertical clusters of void defects or multiple single/connected void defects in close proximity (red elements).

Figure 9: Probabilistic crack paths predicted by ANN (red, green, blue colored symbols) versus actual crack paths (porosity distributions), along with ANN outputs of probabilities at each corresponding crack propagation sequence. Red elements denote void defects.

Figure 10: Snapshots of porosity evolution at increasing K_{I} loading, depicting the formation of unconnected damage zones associated with multiple void interactions for two instantiations of initial void defect distributions (red elements). *Magenta symbols*: ANN-predicted crack paths; *cyan symbols*: ANN-predicted crack paths augmented for isolated damage zone formation.

Figure 11: (**A**) Genetic algorithm (GA) to optimize void defect distribution to achieve crack-path design. (**B**) Evolution of cost function and void defect distributions (red elements) for brittle media.

(**C**) Optimized void defect distributions (red elements) for three different crack designs. *Cyan symbols, magenta symbols, and black-filled elements*: ANN-predicted, targeted, and actual crack paths.

Figure 12: *Above*: Two instantiations of void defect distributions (red elements) with ANN-predicted (cyan symbols) and actual crack paths (porosity distribution). *Below*: Associated fracture resistance curves (solid lines) versus baseline material containing no void defects (dashed lines).

Figure 13: *Above*: Optimized void defect distributions (red elements) to achieve identical crack paths to **Fig. 12**, with targeted (magenta symbols), ANN-predicted (cyan symbols), and actual crack paths (porosity distribution). *Below*: Associated fracture resistance curves (solid lines) versus baseline material containing no void defects (dashed lines).

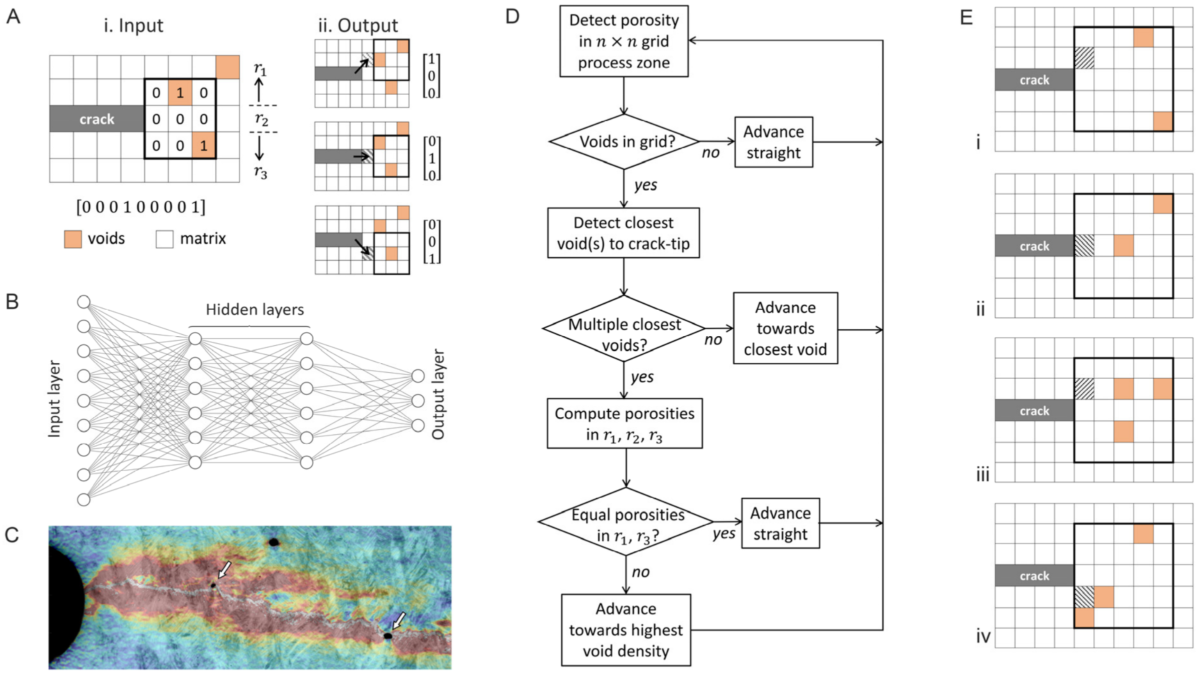

Figure 1: (**A**) Process zone with void defects represented by an $n \times n$ grid of elements (bold solid line region) versus possible crack propagation directions (arrows). (**B**) Artificial neural network (ANN) linking void defect locations within the process zone (input) and the crack propagation direction (output). (**C**) Coalescence of a crack with void defects in additively-manufactured Ti-6Al-4V, resulting in deviation in crack path (VanSickle et al., 2020). (**D**) Flow chart of a rule-based, crack propagation algorithm for brittle fracture. (**E**) Examples of crack propagation direction (patterned element) from given void defect distributions within the process zone.

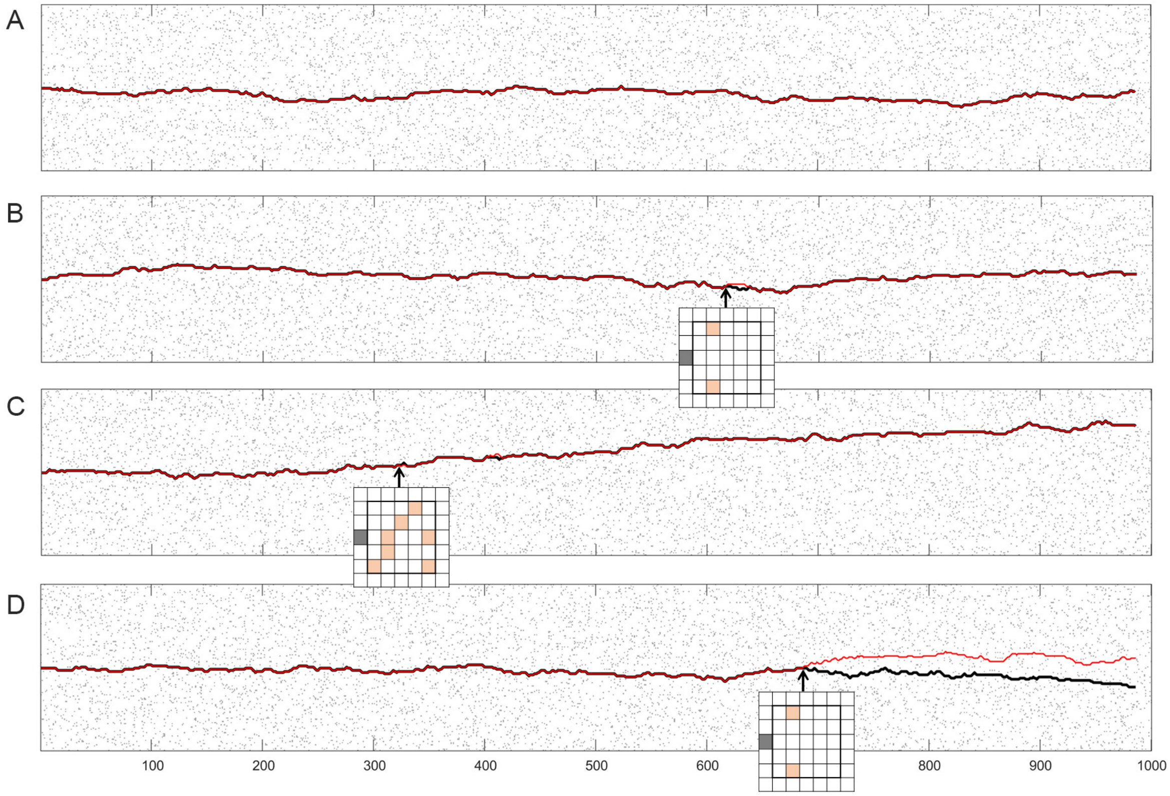

Figure 2: Comparison of the actual (black) versus ANN-predicted crack paths (red) for four instantiations of void defect distributions (grey pixels) with average porosity of 5%. Void defect configuration within the process zone at first instance of crack path deviation denoted by arrows.

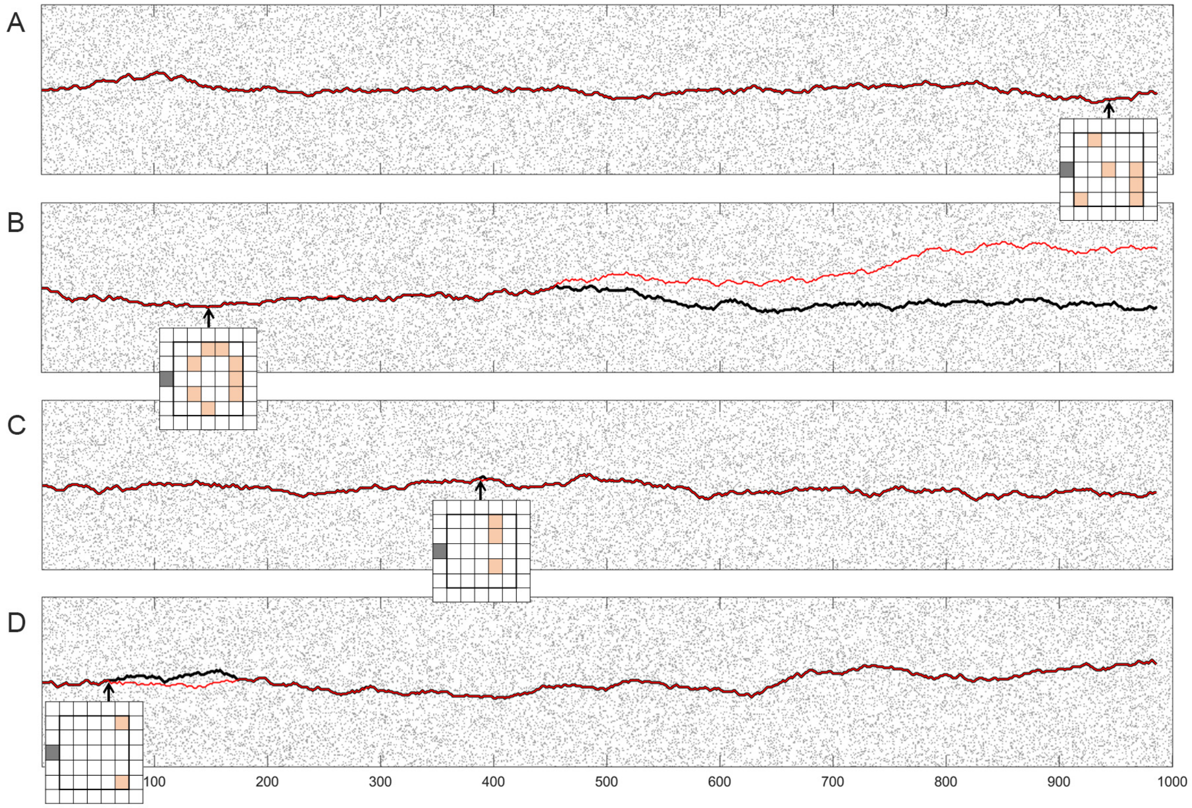

Figure 3: Comparison of the actual (black) versus ANN-predicted crack paths (red) for four instantiations of void defect distributions (grey pixels) with average porosity of 15%. Void defect configuration within the process zone at first instance of crack path deviation denoted by arrows.

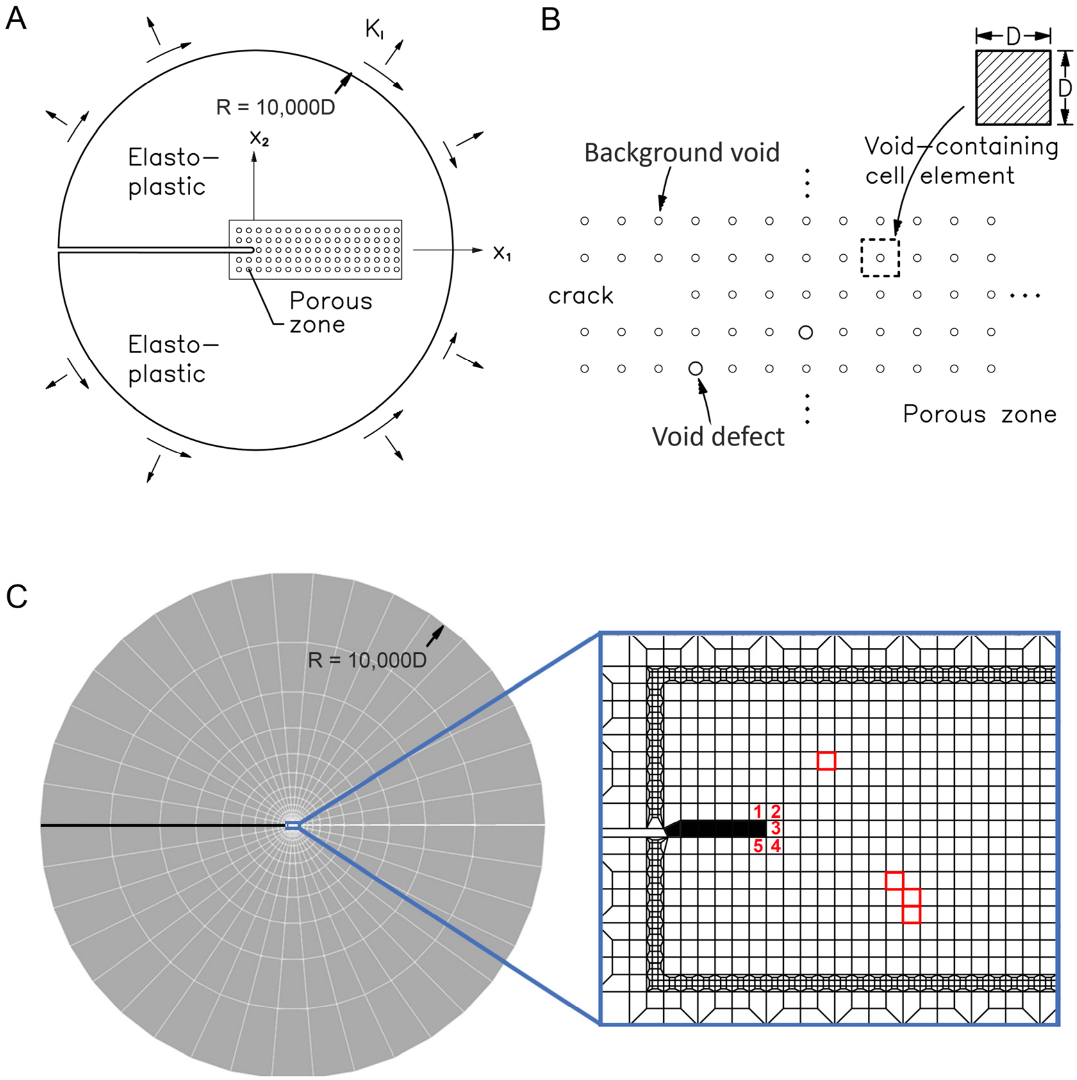

Figure 4: (**A**) Boundary layer model with a centerline crack subjected to mode I K-field loading. (**B**) Schematic of dual-scale porosities comprising of void defects and background voids within a designated porous zone modeled by computational cell elements. (**C**) Finite element mesh of the boundary layer model, with close-up view of the crack (black elements); possible crack propagation directions as marked (1–5), with distribution of isolated or clustered void defects (red elements).

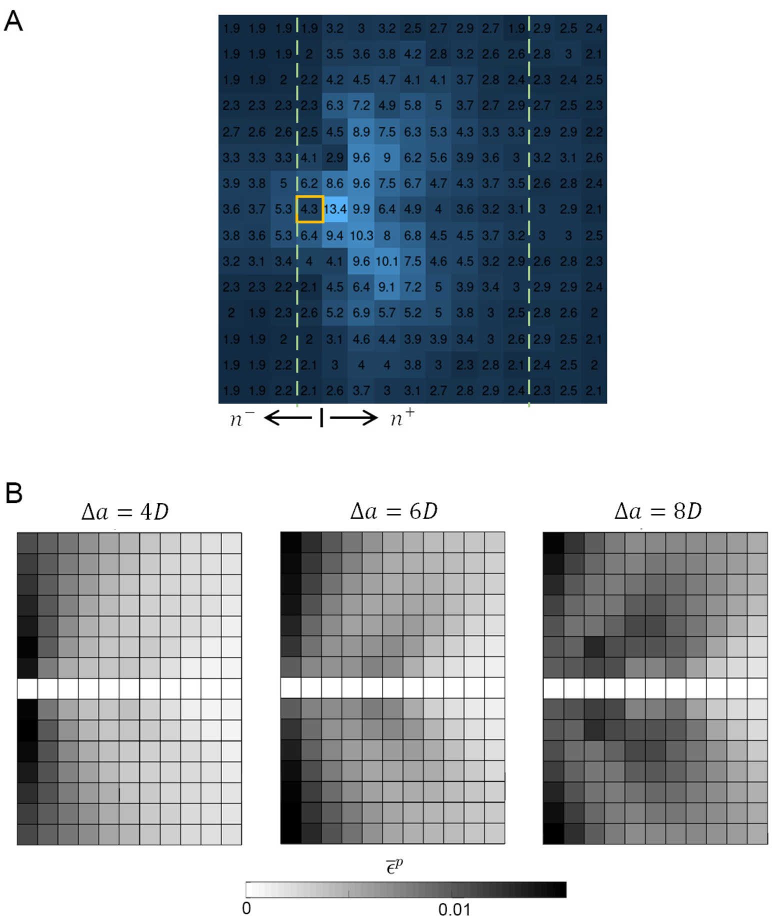

1.9	1.9	1.9	1.9	3.2	3	3.2	2.5	2.7	2.9	2.7	1.9	2.9	2.5	2.4
1.9	1.9	1.9	2	3.5	3.6	3.8	4.2	2.8	3.2	2.6	2.6	2.8	3	2.1
1.9	1.9	2	2.2	4.2	4.5	4.7	4.1	4.1	3.7	2.8	2.4	2.3	2.4	2.5
2.3	2.3	2.3	2.3	6.3	7.2	4.9	5.8	5	3.7	2.7	2.9	2.7	2.5	2.3
2.7	2.6	2.6	2.5	4.5	8.9	7.5	6.3	5.3	4.3	3.3	3.3	2.9	2.9	2.2
3.3	3.3	3.3	4.1	2.9	9.6	9	6.2	5.6	3.9	3.6	3	3.2	3.1	2.6
3.9	3.8	5	6.2	8.6	9.6	7.5	6.7	4.7	4.3	3.7	3.5	2.6	2.8	2.4
3.6	3.7	5.3	4.3	13.4	9.9	6.4	4.9	4	3.6	3.2	3.1	3	2.9	2.1
3.8	3.6	5.3	6.4	9.4	10.3	8	6.8	4.5	4.5	3.7	3.2	3	3	2.5
3.2	3.1	3.4	4	4.1	9.6	10.1	7.5	4.6	4.5	3.2	2.9	2.6	2.8	2.3
2.3	2.3	2.2	2.1	4.5	6.4	9.1	7.2	5	3.9	3.4	3	2.9	2.9	2.4
2	1.9	2.3	2.6	5.2	6.9	5.7	5.2	5	3.8	3	2.5	2.8	2.6	2
1.9	1.9	2	2	3.1	4.6	4.4	3.9	3.9	3.4	3	2.6	2.9	2.5	2.1
1.9	1.9	2.2	2.1	3	4	4	3.8	3	2.3	2.8	2.1	2.4	2.5	2
1.9	1.9	2.2	2.1	2.6	3.7	3	3.1	2.7	2.8	2.9	2.4	2.3	2.5	2.1

Figure 5: (**A**) Contours of two-norm of weights (values as marked) linking elements representing the input nodes to the hidden layer in the ANN. *Yellow element*: current crack-tip; *green boundaries*: final selected process zone. (**B**) Equivalent plastic strain ($\bar{\epsilon}^p$) contours directly ahead of the current crack-tip at three crack lengths (Δa).

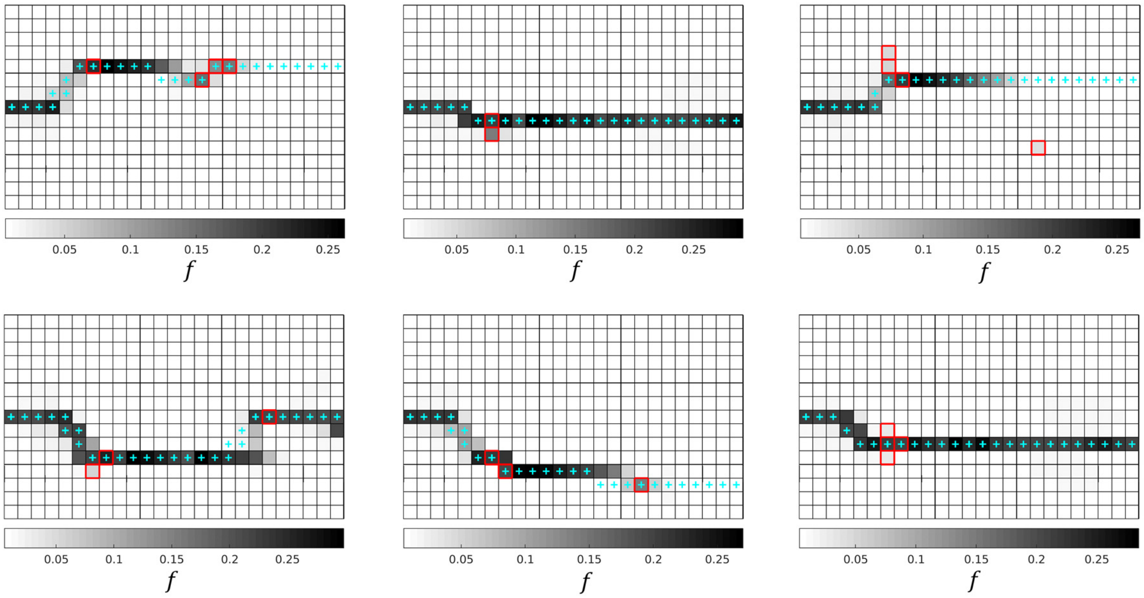

Figure 6: ANN-predicted crack paths (cyan symbols) versus actual crack paths (porosity distributions) for different instantiations of low-density void defects (red elements).

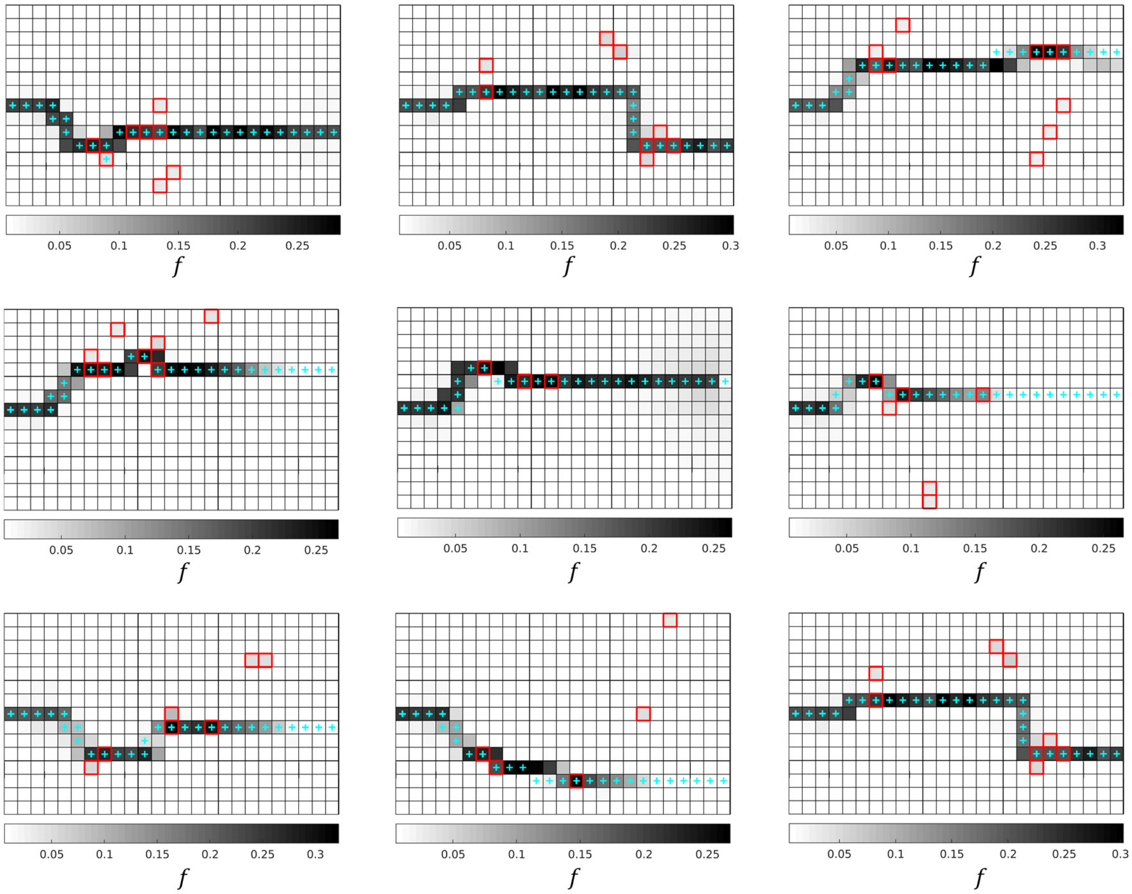

Figure 7: ANN-predicted crack paths (cyan symbols) versus actual crack paths (porosity distributions) for different instantiations of high-density void defects (red elements).

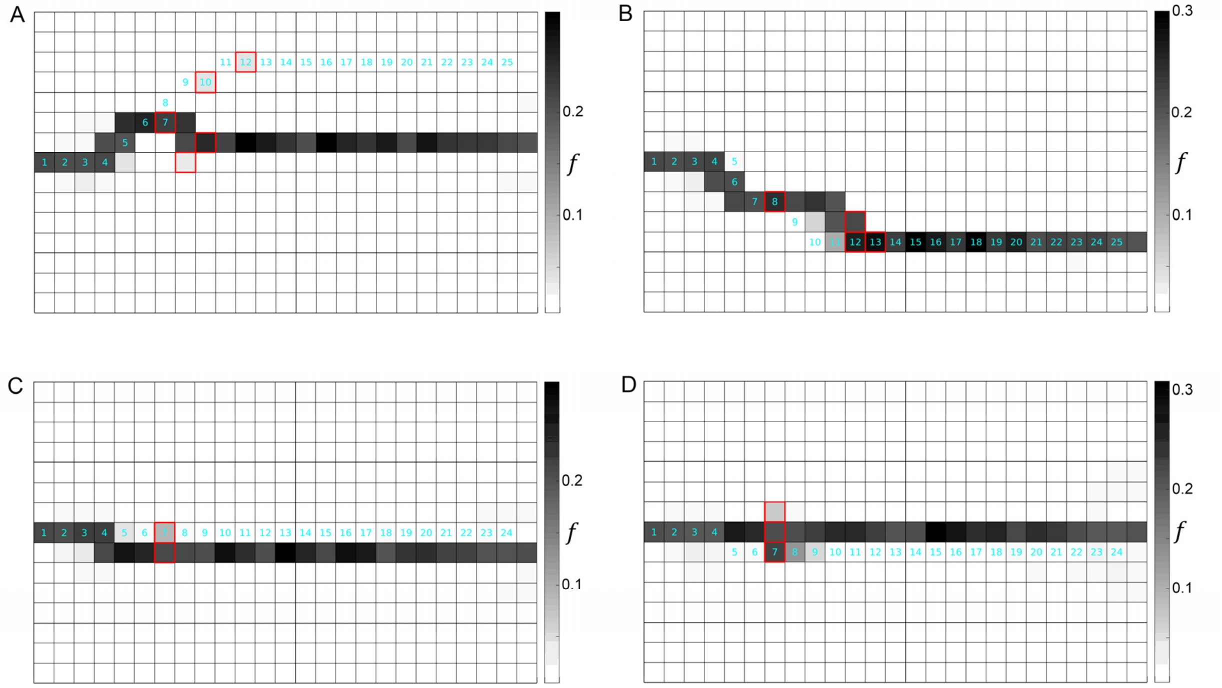

Figure 8: Crack growth sequence (cyan) in ANN-predicted crack paths versus actual crack paths (porosity distributions) in the presence of vertical clusters of void defects or multiple single/connected void defects in close proximity (red elements).

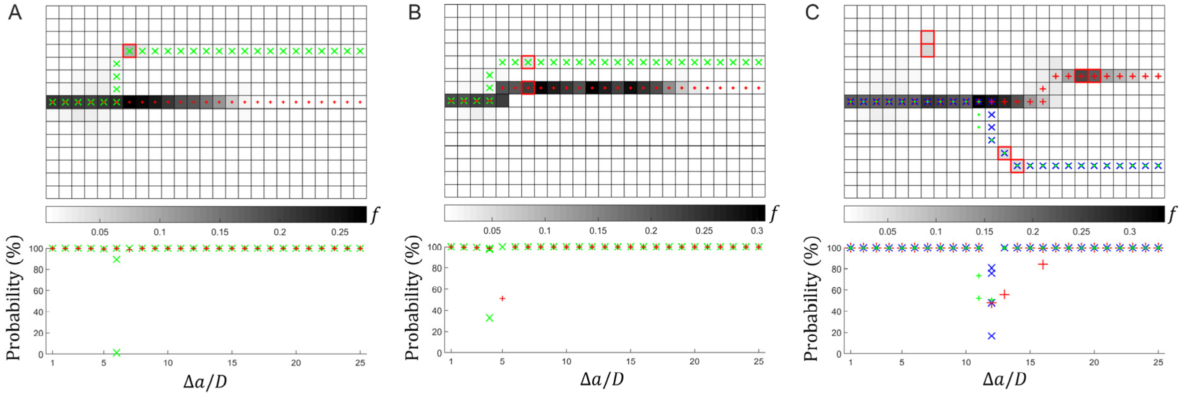

Figure 9: Probabilistic crack paths predicted by ANN (red, green, blue colored symbols) versus actual crack paths (porosity distributions), along with ANN outputs of probabilities at each corresponding crack propagation sequence. Red elements denote void defects.

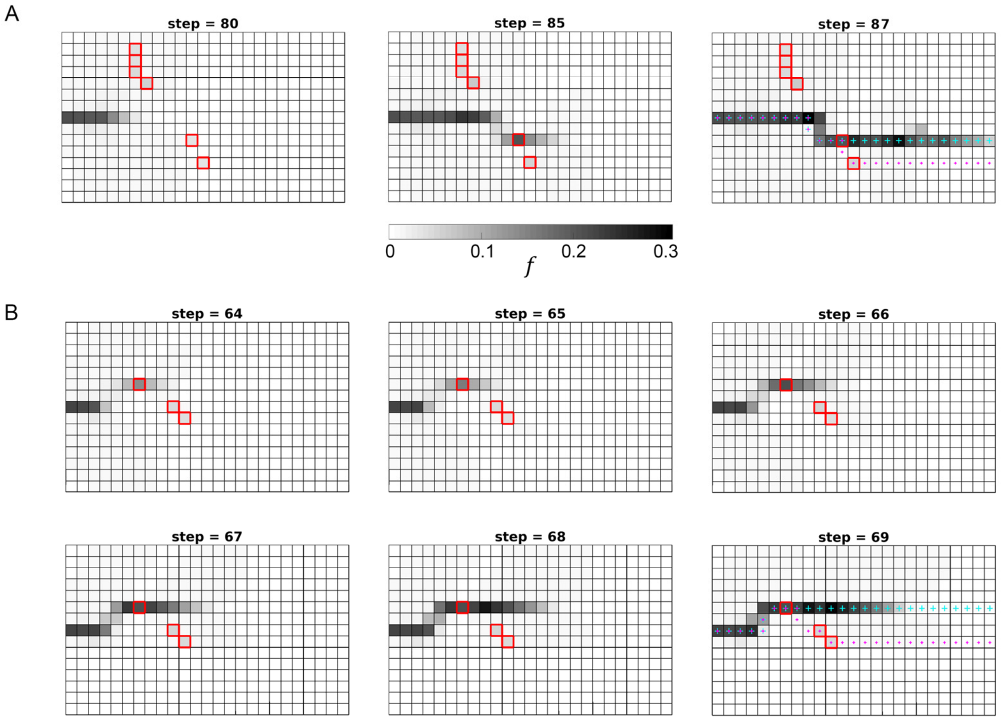

Figure 10: Snapshots of porosity evolution at increasing K_{I} loading, depicting the formation of unconnected damage zones associated with multiple void interactions for two instantiations of initial void defect distributions (red elements). *Magenta symbols*: ANN-predicted crack paths; *cyan symbols*: ANN-predicted crack paths augmented for isolated damage zone formation.

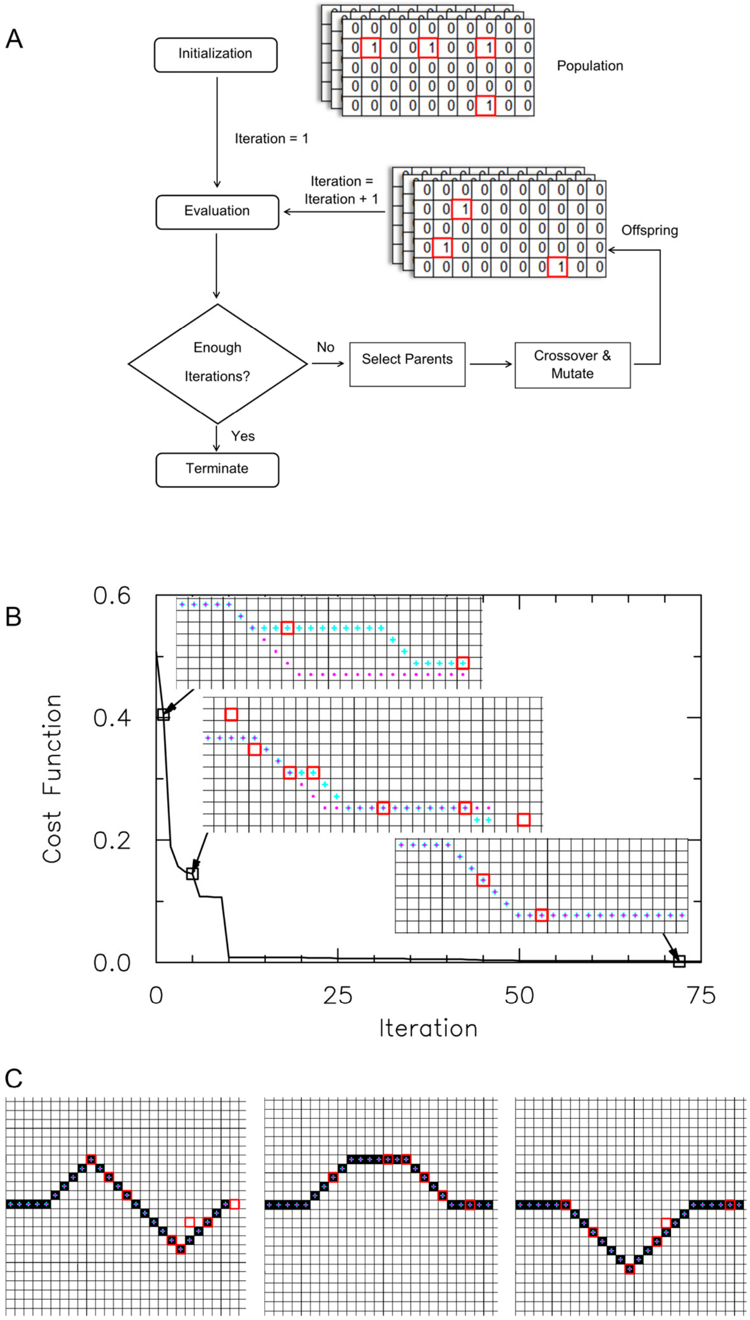

Figure 11: (**A**) Genetic algorithm (GA) to optimize void defect distribution to achieve crack-path design. (**B**) Evolution of cost function and void defect distributions (red elements) for brittle media. (**C**) Optimized void defect distributions (red elements) for three different crack designs. *Cyan symbols, magenta symbols, and black-filled elements*: ANN-predicted, targeted, and actual crack paths.

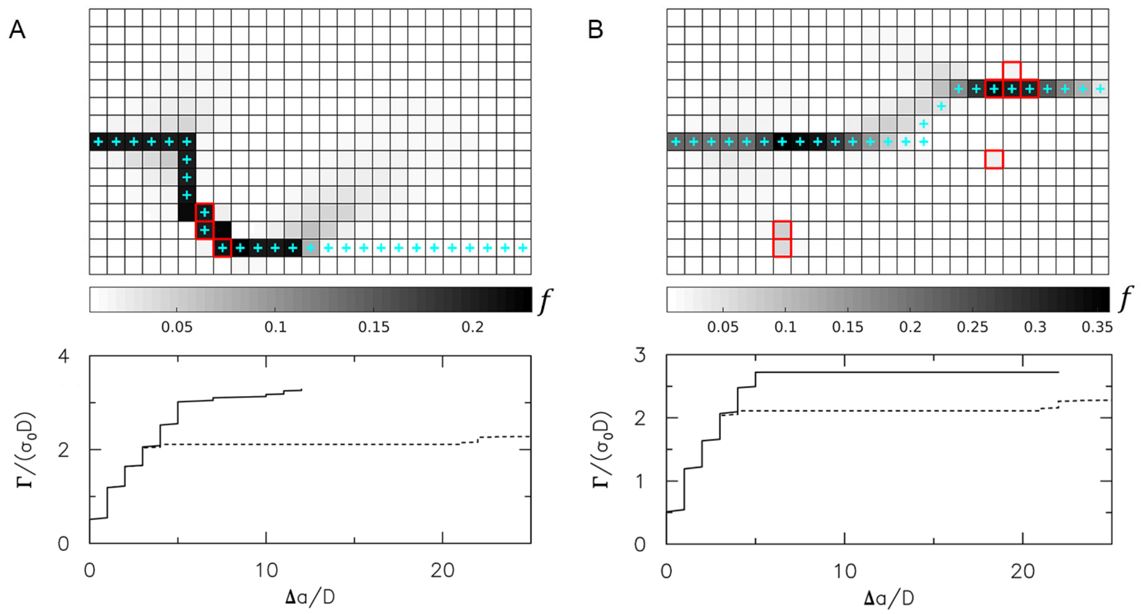

Figure 12: *Above*: Two instantiations of void defect distributions (red elements) with ANN-predicted (cyan symbols) and actual crack paths (porosity distribution). *Below*: Associated fracture resistance curves (solid lines) versus baseline material containing no void defects (dashed lines).

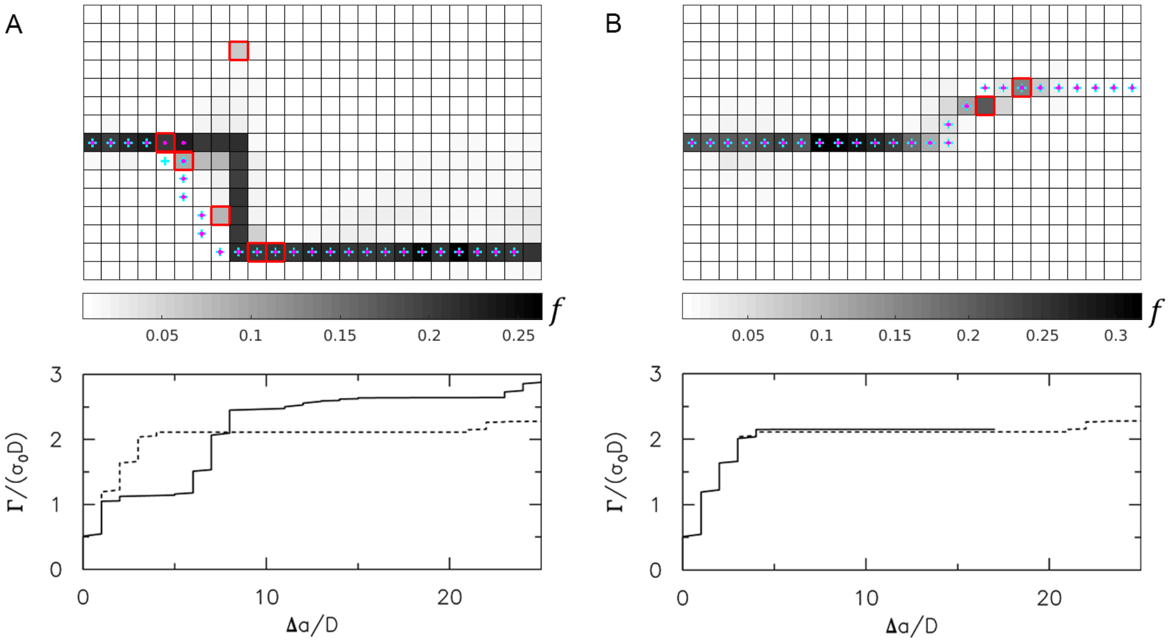

Figure 13: *Above*: Optimized void defect distributions (red elements) to achieve identical crack paths to **Fig. 12**, with targeted (magenta symbols), ANN-predicted (cyan symbols), and actual crack paths (porosity distribution). *Below*: Associated fracture resistance curves (solid lines) versus baseline material containing no void defects (dashed lines).